1788 *Chem. Mater.* **2010,** *22,* 1788–1797
DOI:10.1021/cm903288s

CHEMISTRY OF MATERIALS
Article

Incommensurate Crystallographic Shear Structures and Magnetic Properties of the Cation Deficient Perovskite $(Sr_{0.61}Pb_{0.18})(Fe_{0.75}Mn_{0.25})O_{2.29}$

S. Malo,*,† C. Lepoittevin,†,‡ O. Pérez,† S. Hébert,† G. Van Tendeloo,‡ and M. Hervieu†

†*Laboratoire CRISMAT-ENSICAEN, Bd du Maréchal Juin-14050 CAEN cedex, France and* ‡*EMAT, University of Antwerp, Groenenborgerlaan 171, B-2020 Antwerp, Belgium*

Received October 27, 2009. Revised Manuscript Received December 18, 2009

The origin of the incommensurability in the crystallographic shear (CS) structure of the ferri-Manganite $(Sr_{0.61}Pb_{0.18})(Fe_{0.75}Mn_{0.25})O_{2.29}$, related to the cation deficient perovskite, has been determined by careful analysis of the boundaries between the two variants constituting the phasoid. High Resolution Electron Microscopy/HAADF-STEM images allow the structural mechanisms to be understood through the presence of structural units common to both phases, responsible of the incommensurate character observed in the electron diffraction patterns. The structural analysis allows for identifying different types of CS phases in the Pb−Sr−Fe(Mn)−O diagram and shows that the stabilization of the six-sided tunnels requires a higher A/B cationic ratio. A description of these phases is proposed through simple structural building units (SBU), based on chains of octahedra bordered by two pyramids. The $(Sr_{0.61}Pb_{0.18})(Fe_{0.75}Mn_{0.25})O_{2.29}$ CS compound exhibits a strong antiferromagnetic and insulating behavior, similar to the Fe-2201 and "terrace" ferrites but differs by the presence of a hysteresis, with a small coercive field.

Introduction

The interesting chemical and physical properties of the "ABO_3" perovskite compounds have attracted considerable attention for a long time. A large part of this research has been devoted to their ability to exhibit oxygen (ABO_{3-y}) and/or cation (A_xBO_3) nonstoichiometry mechanisms, which extensively multiply the possible derivative frameworks, easily accommodated through the mixed valence and coordination of the B transition elements.[1,2] Theoretically, the octahedral framework of the ReO_3-type structure ($x = 0$) remains similar to that of the ideal perovskite unit cell, but the existence range of these "deficient perovskites" is often limited to the intermediate values [$1 \geq x > 0.75$]. Note however that in certain of these "A_xBO_3" compounds, such as $CaMn_7O_{12}$[3] or $CaFeTi_2O_6$,[4] the nonstoichiometry is only apparent because the transition metal exhibits at least two oxidation states, the lower one occupying a distorted site with the A cation in an ordered way. In a more general way, the majority of cation deficient compounds are characterized by a breaking of the octahedral framework,[2] as in the bronzes and bronzoids (e.g., $A_{1+x}Nb_3O_9$[5,6]) or the layered "hexagonal" perovskites (e.g., ref 7).

In the pseudobinary system Sr−Fe−O, iron atoms adopt the IV, V, or VI coordinations leading to exceptionally rich systems of oxygen deficient perovskites $SrFeO_{3-y}$, within the existence range $0 < y \leq 0.5$.[8−14] The limit composition $SrFeO_{2.5}$ exhibits a brownmillerite-type structure, where one octahedral layer $[FeO_2]_\infty$ alternates with one tetrahedral layer $[FeO]_\infty$ along $\vec{c}$ (axis of the intergrowth). By doping the Sr site with the isovalent Pb^{2+}, a stoichiometric formula is retained, but the brownmillerite framework is broken by a shear operation along the $(\bar{1}01)_p$ plane in $Pb_{2/3}Sr_{1/3}FeO_{2.5}$[15] (the subscript p denotes the perovskite subcell).

Different investigations of the cation deficient A_xBO_{3-y} systems, with A = Sr and post-transition cations (Pb^{2+}, Tl^{3+}, and Bi^{3+}) and B = Fe and Mn, showed two structural

*Corresponding author e-mail: sylvie.malo@ensicaen.fr.

(1) Galasso, S. *Structure, properties and preparation of perovskite type compounds*; Pergamon Press: Oxford, U.K., 1969.
(2) Mitchell, R. H. *Perovskites, modern and ancient*; Almaz Press: Thunder Bay, ON, Canada, 2002.
(3) Bochu, B.; Chenavas, J.; Joubert, J. C.; Marezio, M. *J. Solid State Chem.* **1974**, *11*, 88.
(4) Leinenweber, K.; Parise, J. *J. Solid State Chem.* **1995**, *114*, 277.
(5) Torardi, C. C.; Brixner, L;H.; Foris, C. M. *J. Solid State Chem.* **1985**, *58*, 204.
(6) Abakumov, A. M.; Shpanchenko, R. V.; Antipov, E. V. *Mater. Res. Bull.* **1995**, *30*, 97.
(7) Darriet, J.; Subramanian, M. A. *J. Mater. Chem.* **1995**, *5*, 543.
(8) Bertaut, E. F.; Blum, P.; Sagnieres, A. *Acta Crystallogr.* **1959**, *12*, 149.
(9) Takeda, Y.; Kanno, K.; Takada, T.; Yamamoto, O.; Takano, M.; Nakayama, N.; Bando, Y. *J. Solid State Chem.* **1986**, *63*, 237.
(10) Grenier, J. C.; Ea, N.; Pouchard, M.; Hagenmuller, P. *J. Solid State Chem.* **1985**, *58*, 243.
(11) Takano, M.; Okita, T.; Nakayama, N.; Bando, Y.; Takeda, Y.; Yamamoto, O.; Goodenough, J. B. *J. Solid State Chem.* **1988**, *73*, 140.
(12) Hodges, J. P.; Short, S.; Jorgensen, J. D.; Xiong, X.; Dabrowski, B.; Mini, S.; Kimball, C. W. *J. Solid State Chem.* **2000**, *151*, 190.
(13) Greaves, C.; Jacobson, A;J.; Tofield, B. C.; Fender, B. E. F. *Acta Crystallogr., Sect. B: Struct. Sci.* **1975**, *B31*, 641.
(14) Takeda, T.; Yamaguchi, Y.; Watanabe, H. J. *Phys. Soc. Jpn.* **1972**, *33*, 967.
(15) Raynova-Schwarten, V.; Massa, W.; Babel, D. *Z. Anorg. Allg. Chem.* **1997**, *623*, 1048.

 Published on Web 01/19/2010

families of related perovskite compounds. The first one belongs to the layered structures, which can be described, by reference to the superconducting oxides,[16] as an intergrowth of m perovskite layers with one triple rock salt block, according to the general formula $Fe_2(Sr_{2-y}A_y)Sr_{m-1}Fe_mO_{3m+3.5-\delta/2}$ and denoted Fe-22(m-1)m[17−22]. It was also shown that increasing the Pb^{2+} content in these framework provokes shear mechanisms with the formation of a "terrace" structure for the composition $(Sr_{0.54}Pb_{0.17})FeO_{2.21}$.[23] The second family is characterized by modulated 1/2[110](*h0l*) crystallographic shear (CS) structures in the Pb−Sr−Fe−O system, according to the formula $Pb_{4m+3n}Fe_{4(m+n)}O_{10m+9n}$[24−26] and in the Pb−Mn−O system.[27] A brief state of the art on these complex materials is given in the first section of the present paper.

Recently, a new Sr rich compound $(Sr_{0.61}Pb_{0.18})(Fe_{0.75}Mn_{0.25})O_{2.29}$ has been synthesized, which exhibits a $1/2[110]_p(203)_p$ crystallographic shear structure.[28] However, HRTEM and HAADF-STEM evidenced an original characteristic with a matrix built on the coexistence of two phases having the same monoclinic supercell but slightly different structures. The difference is situated in the so-called "translational interface" of the framework, with the local formation of single six-sided tunnels occupied by two columns of Pb^{2+} cations in the phase "1" (tunnels labeled "H" in ref 29) and two six-sided tunnels "H" in the phase "2". As a result, the structure has been described as a phasoid.[30] However, an electron microscopy investigation of numerous crystallites revealed that losses of the periodicity are locally observed, depending on the selected area.

The aim of this paper is to determine the origin of the incommensurability in the ferri-manganite $(Sr_{0.61}Pb_{0.18})(Fe_{0.75}Mn_{0.25})O_{2.29}$, the nature of the junctions between the two variants and the nanostructural mechanisms operating. The structural relationship between the different ferrites Fe-22(m-1)m and the Pb-site deficient perovskite-related compounds $Pb_{4m+3n}Fe_{4(m+n)}O_{10m+9n}$ are discussed, and their magnetic properties are presented.

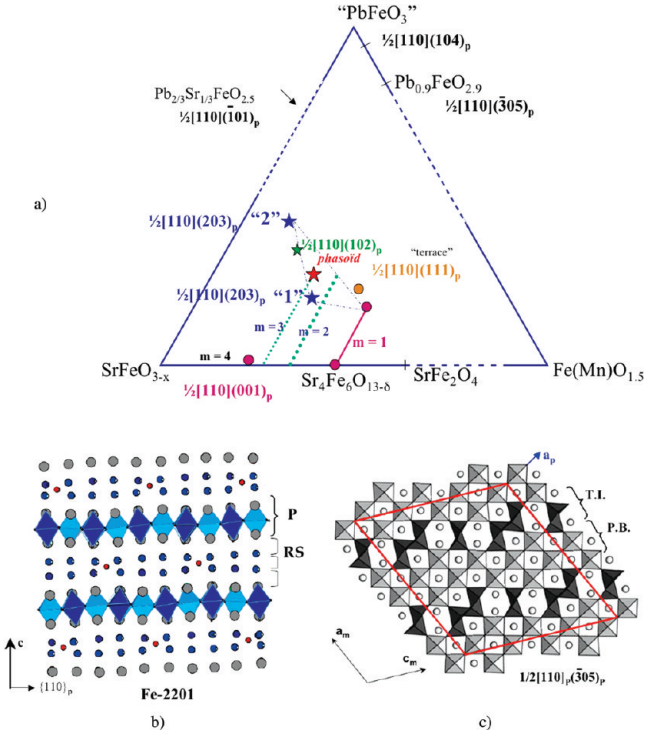

Figure 1. a) Part of the Pb−Sr−Fe(Mn)O diagram (stars are associated with CS structures exhibiting five- and six-sided tunnels and full circles to the Fe-22 nm type structures). Projections along [010] of b) the Fe-2201 structure $Sr_4Fe_6O_{13-\delta}$. The oxygen atoms of the double iron layer are omitted, except the ones directly associated with the modulated structure (red atom) and c) the $1/2[110]_p(\bar{3}05)_p$ CS structure of $Pb_{18}Fe_{20}O_{48}$.

State of the Art: The Layered Fe_22(m-1)m and the 1/2[110](*h0l*) CS Deficient Structures. The main structures discussed in the present paper are represented in the pseudoternary diagram Pb−Sr−Fe(Mn)−O in Figure 1a. The existence domain of the perovskite related Sr-deficient phases, $Sr_{1-x}FeO_{2.5-y}$, ranges between $0 < x \leq 1/3$. The lower limit $x = 1/3$, with the theoretical composition $Sr_{2/3}FeO_{2.167}$, is the only single-phased compound stabilized at present. It corresponds in fact to the $Sr_4Fe_6O_{13-\delta}$ phases, characterized by different incommensurate modulated structures having wavelengths correlated to the exact oxygen content (i.e., to δ).[16−18] Along $\vec{c}$, one perovskite-type slice $[SrFeO_3]_\infty$ alternates with one complex triple rock salt-type block $[SrFe_2O_{3.5-\delta/2}]_\infty$, so that the structure can be associated with a 2201-type structure (notation adopted for the superconducting cuprates and related[19]). This structure is schematically projected along [010] in Figure 1b, the oxygen atoms of the double iron layer being omitted, except the ones directly associated with the modulated structure. Increasing the thickness of the perovskite slice leads to the formation of a family of new materials, denoted Fe-22(m-1)m, with the members $m = 2$ (Fe-2212) and $m = 4$ (Fe-2234).[20,21] The structure refinements carried out in the 4D formalism[22] showed three types of iron polyhedra (square pyramids, trigonal bipyramids, and monocaped tetrahedra) in the double iron layer $[Fe_2O_{2.5-\delta/2}]_\infty$ of the triple rock salt layer. As discussed further, these structures can be also considered as complex crystallographic shear

(16) Raveau, B.; Michel, C.; Hervieu, M.; Groult, D. *Crystal chemistry of High Tc superconducting copper oxides*; Springer-Verlag: Berlin-New York, 1991; Springer Series in Materials Science 15.
(17) Kanamuru, F.; Shimada, M.; Koizumi, M. *J. Phys. Chem. Solids* **1972**, *33*, 1169.
(18) Mellenne, B.; Retoux, R.; Lepoittevin, C.; Hervieu, M.; Raveau, B. *Chem. Mater.* **2004**, *16*, 5006.
(19) Rossell, D.; Abakumov, A. M.; Van Tendeloo, G.; Pardo, J. A.; Santiso, J. *Chem. Mater.* **2004**, *16*, 2578.
(20) Grebille, D.; Lepoittevin, C.; Malo, S.; Pérez, O.; Nguyen, N.; Hervieu, M. *J. Solid State Chem.* **2006**, *179*, 3849.
(21) Lepoittevin, C.; Malo, S.; Nguyen, N.; Hébert, S.; Van Tendeloo, G.; Hervieu, M. *Chem. Mater.* **2008**, *20*, 6468.
(22) Pérez, O.; Mellenne, B.; Retoux, R.; Raveau, B.; Hervieu, M. *Solid State Sci.* **2006**, *8*, 431.
(23) Lepoittevin, C.; Malo, S.; Pérez, O.; Nguyen, N.; Maignan, A.; Hervieu, M. *Solid State Sci.* **2006**, *8*, 1294.
(24) Abakumov, A.; Hadermann, J.; Bals, S.; Nikolaev, I. V.; Antipov, E.; Van Tendeloo, G. *Angew. Chem., Int. Ed.* **2006**, *45*, 6697.
(25) Hadermann, J.; Abakumov, A.; Nikolaev, I. V.; Antipov, E.; Van Tendeloo, G. *Solid State Sci.* **2008**, *10*, 382.
(26) Abakumov, A.; Hadermann, J.; Van Tendeloo, G.; Antipov, E. *J. Am. Ceram. Soc.* **2008**, *91*, 1807.
(27) Bougerol, C.; Gorius, M. F.; Grey, I. E. *J. Solid State Chem.* **2002**, *169*, 131.
(28) Lepoittevin, C.; Hadermann, J.; Malo, S.; Pérez, O.; Van Tendeloo, G.; Hervieu, M. *Inorg. Chem.* **2009**, *48*, 8257.
(29) Lepoittevin, C.; Malo, S.; Van Tendeloo, G.; Hervieu, M. *Solid State Sci.* **2009**, *11*, 595.
(30) Magneli, A. *Microsc. Microanal. Microstruct.* **1990**, *1*, 299.

Table 1. Dual Formulation of the Different Compounds Represented on the Diagram (Figure 1a) and Discussed Herein

formulation per cell	cation deficient perovskite	$1/2[110](h0l)_p$	ref	label
$Fe_2(Sr_{2-x}Pb_x)FeO_{6.5-\delta/2}$	$(Sr_{2/3-x}Pb_x)FeO_{2.167}$	$1/2[110](001)_p$	[16−18]	Fe-2201
$Sr_{20}Pb_4Fe_{26}O_{63}$	$(Sr_{0.54}Pb_{0.12})FeO_{2.167}$		29	
$Fe_2(Sr_{2-x}A_x)SrFe_2O_{9.5-\delta/2}$	$(Sr_{0.75-x}A_x)FeO_{2.375}$	$1/2[110](001)_p$	20	Fe-2212
$Fe_2(Sr_{2-x}A_x)Sr_3Fe_4O_{14.65}$	$(Sr_{0.83-x}A_x)FeO_{2.44}$	$1/2[110](001)_p$	21	Fe-2234
$Sr_{13}Pb_4Fe_{24}O_{53}$	$(Sr_{0.54}Pb_{0.17})FeO_{2.21}$	$1/2[110]_p(111)_p$	23	terrace
$Pb_{18}Fe_{20}O_{48}$	$Pb_{0.9}FeO_{2.4}$	$1/2[110]_p(\bar{3}05)_p$	24	
$Pb_4Sr_2Fe_6O_{15}$	$(Sr_{2/3}Pb_{1/3})FeO_{2.21}$	$1/2[110]_p(\bar{1}01)_p$	15	stoichiometric
$Pb_{15}Fe_{16}O_{39}$	$Pb_{0.938}FeO_{2.438}$	$1/2[110]_p(104)_p$	25	
$Sr_{17}Pb_5Fe_{21}Mn_7O_{63}$	$(Sr_{0.61}Pb_{0.18})(Fe_{0.75}Mn_{0.25})O_{2.29}$	$1/2[110]_p(203)_p$	28	phasoid
$Sr_{18}Pb_4(Fe,Mn)_{28}O_{64}$	$(Sr_{0.64}Pb_{0.14})(Fe_{0.75}Mn_{0.25})O_{2.29}$	$1/2[110]_p(203)_p$	28	phase "1"
$Sr_{16}Pb_8(Fe,Mn)_{26}O_{63}$	$(Sr_{0.62}Pb_{0.31})(Fe_{0.75}Mn_{0.25})O_{2.43}$	$1/2[110]_p(203)_p$	[28]	phase "2"
$Sr_{10}Pb_4(Fe,Mn)_{16}O_{63}$	$(Sr_{0.71}Pb_{0.25})(Fe,Mn)O_{2.375}$	$1/2[110]_p(102)_p$	this work	

structures (see the last section). In the Sr-rich part of the Pb−Sr−Fe−O diagram (Figure 1a), the formation of complex crystallographic shear (CS) planes has been also observed for $(Sr_{0.54}Pb_{0.17})FeO_{2.21}$,[23] described as the intergrowth of Fe-2201 and Fe-2212 structures. In this paper, the formulation of the different compounds is given in terms of a CS structure as well as in terms of a cation deficient perovskite; the relationships are brought together in Table 1.

CS structures of ferrites and manganites have been first discovered in the lead rich part of the diagram (Figure 1a). The large family of Pb-site deficient perovskite-related compounds $Pb_{4m+3n}Fe_{4(m+n)}O_{10m+9n}$[24−26] consists of different modulated $1/2[110](h0l)_p$ CS structures having the same average pseudocubic unit cell with $a \approx a_p$ (a_p is the parameter of the perovskite unit cell), a modulation vector $\vec{q} = \alpha\vec{a}^* + \gamma\vec{c}^*$, and the superspace group $X2/m(\alpha 0\gamma)$ with a centring vector [1/2,1/2,1/2,1/2]. The detailed shear operation, which generates these CS structures, has been previously described.[15,24] The $1/2[110]_p$-$(\bar{3}05)_p$ CS structure of $Pb_{18}Fe_{20}O_{48}$ ($Pb_{0.9}FeO_{2.4}$)[24] is taken as an example in Figure 1c for describing the structure-type of the members of the Pb-site deficient perovskite-related compounds. The perovskite (P) "slice" located in between two CS planes forming the "translational interface" (T.I.) has an average thickness of two BO_6 octahedra (B = Fe). The BO_6 octahedra of the perovskite layers and four pentagonal pyramids BO_5 manage six-sided tunnels in the translational interface, where two columns of Pb^{2+} cations are located.

The electron diffraction investigation of the $(Sr_{0.61}Pb_{0.18})(Fe_{0.75}Mn_{0.25})O_{2.29}$ compound[28] has evidenced the existence of two types of patterns, associated with commensurate and incommensurate modulations, so that the description of the patterns implied the introduction of a modulation vector ($p\vec{a}^* + r\vec{c}^*$) with each reflection indexed $ha_p^* + kb_p^* + lc_p^* + mq$ with h,k,l,m integer. The commensurate structure was described using the vector $q = 2/25a_p^* + 3/25c_p^*$, with the centering vector [1/2 1/2 1/2 1/2] and the $I2/m(p0r)$ superspace group. The parameters of the monoclinic supercell of $(Sr_{0.61}Pb_{0.18})$-$(Fe_{0.75}Mn_{0.25})O_{2.29}$ have been refined[28] from powder X-ray diffraction data to $a_m = 27.595(2)$ Å, $b_m = 3.8786(2)$ Å, $c_m = 13.3453(9)$ Å, and $\beta_m \approx 100.126(5)°$ (the subscript m denotes the monoclinic supercell). Due to the complex nanostructure of the $(Sr_{0.61}Pb_{0.18})(Fe_{0.75}Mn_{0.25})O_{2.29}$ phasoid with the existence of two variants associated with the commensurate structure, only the latter was documented in our previous paper.[28] Each of the two variants exhibits a $1/2[110]_p(203)_p$ crystallographic shear (CS) (Figure 2a). The phase "1" is characterized by the existence of single tunnels "H" bordered by two groups of four edge sharing pyramids, the structural unit B_4O_{14}; two pentagonal cages are managed between two adjacent B_4O_{14} units. The phase "2" is characterized by the existence of two tunnels "H" which share a B_2O_8 unit built up from two edge sharing pyramids and are bordered by two groups of B_4O_{14} structural units. The two "translational interfaces" differ by the sequences of the six-sided tunnels and the groups of edge sharing pyramids located in between, which can be characterized as follows (Figure 2a)

phase″1″ :

-one tunnel″H″-one unit B_4O_{14}-one unit B_4O_{14}

phase″2″ :

-one tunnel″H″-one unit B_2O_8-one unit″H″-one unit B_4O_{14}

As a result, the main difference between the two variants is in fact the occupancy factor of 2 atomic sites, schematically drawn in Figure 2b. The first site is occupied either by the B cation of a BO_5 pyramid (B = Fe or Mn) in phase "1" or by an A^{2+} cation (likely Pb^{2+}) in phase "2". The second site is an oxygen position which is empty or fully occupied, transforming a BO_5 pyramid in phase "1" into a BO_6 octahedron in phase "2" (small vertical arrow). The theoretical compositions per monoclinic cell are $Sr_{18}Pb_4(Fe,Mn)_{28}O_{64}$ for the phase "1" and $Sr_{16}Pb_8(Fe,Mn)_{26}O_{63}$ for the phase "2". The two limit models therefore exhibit the same amount of cations, Pb+Sr+(Fe+Mn) = 50. The presence of these two variants in the form of nanophases has justified the description of the material as a phasoid [28], with the general formula of the average structure $Sr_{16}Pb_4(Fe+Mn)_{26}$-$\mathbf{M}_4O_{63\pm\varepsilon}$, with M being any cation of the framework as shown in Figure 2b. It is important to recall that these two formulas correspond to the hypothesis that the cations located in the six-sided tunnels "H" are only Pb^{2+} and that all the others, namely five-sided tunnels and perovskite cages, are only occupied by Sr^{2+}; they are supposed to simplify the description of the models and

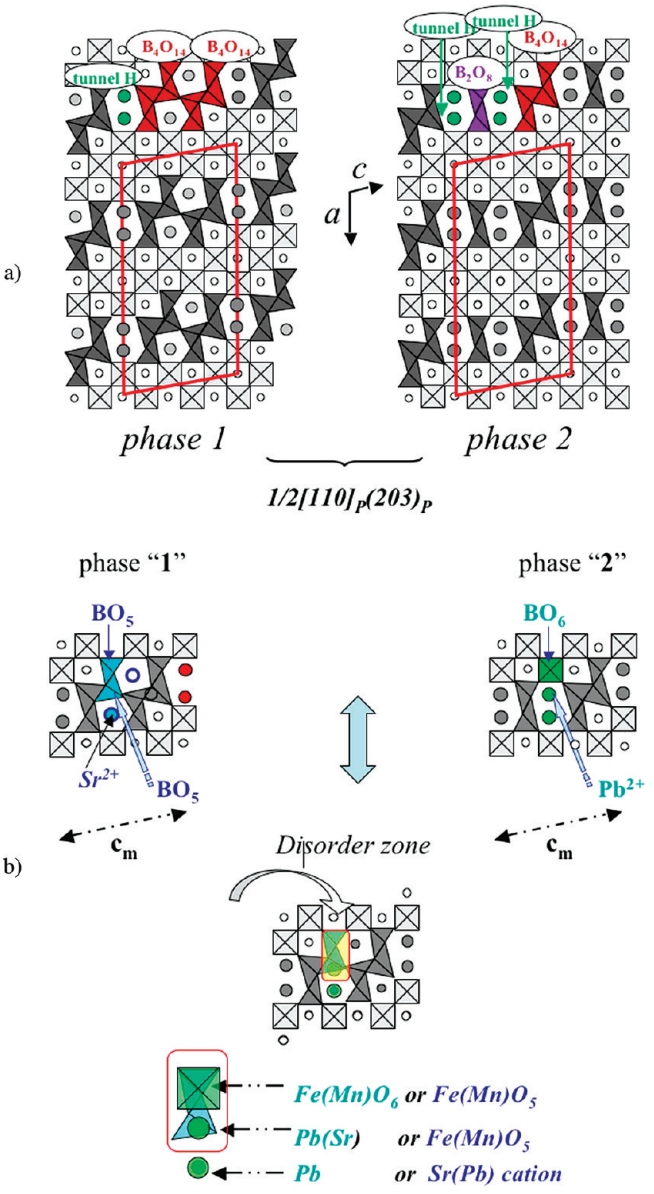

Figure 2. Projections along [010] of the $1/2[110]_p(203)_p$ CS structure of a) the phase "1" $Pb_4Sr_{18}(Fe,Mn)_{28}O_{64}$ and phase "2" $Pb_8Sr_{16}(Fe,Mn)_{26}O_{63}$ and b) the differences at the level of the interface between the ordered "1" and "2" structures and representation of the average structure of the phasoid.

structural mechanisms since the results obtained in the diagram show that the two cations are both able to occupy the different sites in these complex frameworks.

Experimental Section

The powder compound was prepared in a glovebox starting from PbO, SrO, Fe_2O_3, and Mn_2O_3 in the stoichiometric ratio. The mixture was then pressed into bars, sealed in a silica tube, heated at 1100 °C for 48 h with a heating rate of 1.5 °C/min, and slowly cooled at the same rate. More details can be found in ref 28.

Energy dispersive analyses carried out on 50 crystallites evidenced an average cation ratio of $Sr_{17}Pb_5Fe_{21}Mn_7$, and electron diffraction confirmed the CS nature of the crystallites.[28] No secondary phase has been detected from the X-ray powder diffraction (XRPD) study. The synthesis conditions are consistent with a trivalent oxidation state of the Mn and Fe cations (confirmed by redox titration), so that the composition $Sr_{17}Pb_5(Fe_{21}Mn_7)O_{63\pm\varepsilon}$ has been proposed.

The structural study was carried out by transmission electron microscopy (TEM). A small piece of sample was crushed in an agate mortar containing n-butanol, and a droplet was deposited on a copper grid covered with holey carbon film. Electron diffraction (ED) was carried out with a JEOL 200 CX microscope. The microscope used for high resolution TEM (HRTEM) was a JEOL 4000EX operating at 400 kV. The Z-contrast images were obtained on a JEOL 3000F microscope working in scanning transmission mode (STEM) unit, and images were recorded using a high-angle annular dark field (HAADF) detector. High-resolution images were simulated using the Mac Tempas software.

The magnetization measurements were carried out in a SQUID magnetometer (Quantum Design).

Results

The description of the material in the form of nanodomains of two phases forming a phasoid[28] was a first and important approach of its real nature, but this description does not allow all the experimental observations to be explained. They especially deal with the existence of ED patterns exhibiting a weak deviation with regard to the commensurate supercell, although the two variants are characterized by a similar unit cell. The global symmetry of the ED pattern is monoclinic, and the reflection conditions are in agreement with the centering vector [1/2 1/2 1/2 1/2].

The ED pattern of the commensurate structure (a_m = 27.595(2) Å, b_m = 3.8786(2) Å, c_m = 13.3453(9) Å, and $\beta_m \approx 100.126(5)°$) is schematically drawn in Figure 3a with the satellites (red dots) of the commensurate modulation vector along the $[203]_p^*$ direction of the perovskite subcell (blue dots and subscript p). Two enlarged schemes allow understanding the indexation of the pattern using the four indices $hklm$. The lower one represents the monoclinic unit cell in the form of a red rectangle with $\vec{a}_m^*$ parallel to the $[203]_p^*$ direction and $\vec{c}_m^*$ parallel to the $[10\bar{1}]_p^*$ direction; it corresponds to $a_m^* = H_{0001}$, $b_m^* = b^*$, and $c_m^* = H_{10\bar{1}\bar{1}0}$. The enlarged scheme (upper one) represents the 101_p and 200_p basic reflections of the perovskite subcell and the satellites located in between. The particular values of $q = 2/25a_p^* + 3/25c_p^*$ involve that four satellites are aligned along $[10\bar{1}]_p^*$ with the basic reflections of the perovskite subcell and regularly spaced (see the yellow area). All reflections are indexed in this enlarged scheme. Note that for this commensurate structure each of these spots is the superposition of two satellites, the sum $\sum|m|$ of the m values of two associated $hklm$ satellites, $\bar{2}04\bar{4}0/20\bar{2}\bar{1}0$ or $\bar{1}0\bar{3}30/303\bar{2}0$ for example, is 50, i.e. the order along the $[203]_p^*$ direction.

In the experimental patterns of incommensurate modulations (Figure 3b), the aperiodicity is clearly detected from the positions of the satellites, which are no longer aligned along the rows parallel to $[10\bar{1}]_p^*$, with unequal interspot distances. This is highlighted in the enlarged scheme in Figure 3b, which presents a zone of the pattern equivalent to that of the commensurate phase in Figure 3a

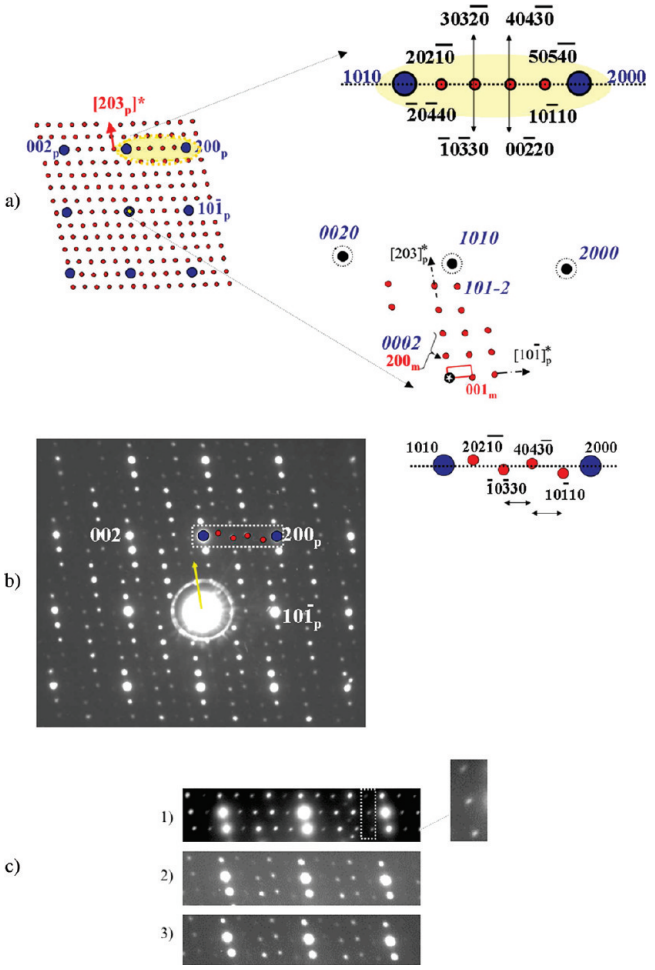

Figure 3. a) Ideal and schematic [010] ED patterns of the commensurate structure, with the perovskite reflections (blue dots) and satellites (red dots). The bottom-enlarged scheme presents the monoclinic unit cell and the indexation using four *hklm* indices. The yellow part of the pattern, between the 101_p and the 200_p reflections, is enlarged to highlight that the two basic reflections and satellites are aligned. b) Experimental [010] pattern characteristic of an incommensurate modulated structure. The satellites located between the 1010 and 2000 reflections are enlarged in the right part of the pattern; only the visible satellites are indexed. c) Example of three patterns showing the satellites evolution with q.

(follow the dotted line). The intensity decrease of the satellites close to the basic reflections, independently of the dynamic effect, is another phenomenon associated with this loss of the commensurability. It is correlated to the fact that the couples of satellites are disassociated in the incommensurate structures; only the more intense satellites are indexed in the enlarged scheme. In the experimental ED pattern of Figure 3b, the modulation wave vector is approximately $q = 0.0787a_p^* + 0.1179c_p^*$. The evolution of both the position and intensity of the satellites is illustrated in Figure 3c, where the corresponding zones of three patterns have been enlarged. Different relative positions are indeed possible for the satellites, as a function of the p and r components of the modulation vector. In Figure 3c1, the aperiodicity is barely visible (p and r remain very close to 0.08 and 0.12) and is only detectable by the elongated form of the satellites close to the basic reflections (see enlarged part): this elongation results from a tiny displacement of the two associated

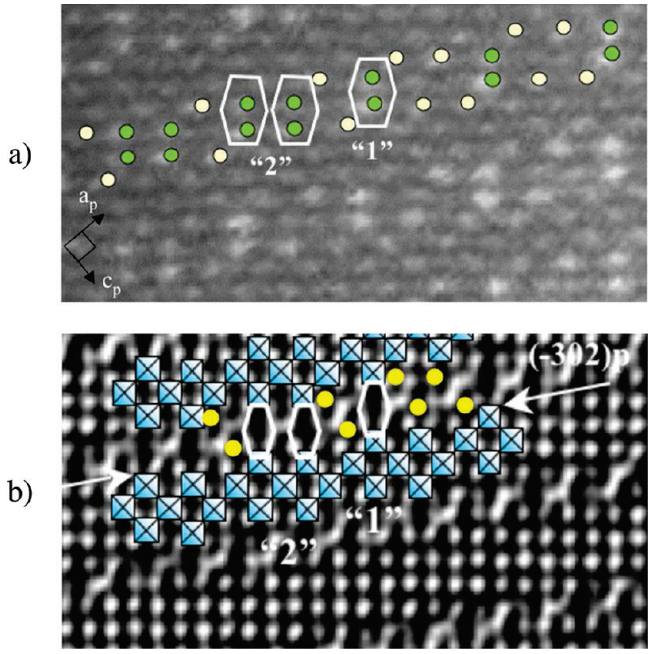

Figure 4. Compared enlarged [010] images to outline the complementarities information of (a) HAADF STEM and (b) HRTEM.

satellites (as $505\overline{4}0$ and $10\bar{1}10$ for the circled spot) as soon as p is different from 2/25 or r from 3/25. The experimental pattern ($p = 0.0787$ and $r = 0.118$) is enlarged in Figure 3c3, whereas in Figure 3c2 an intermediate one with $p = 0.0797$ and $r = 0.118$ is represented. It clearly appears that these values remain very close to those of the commensurate $1/2[110]_p(203)_p$ structures.

HREM and HAADF-STEM Observations. In this study, we have only considered the recurrent nonstoichiometry phenomena, which could be considered as significant to explain the incommensurate modulation observed in the ED patterns. As previously shown,[28] the high resolution electron microscopy (HRTEM) and high-angle annular dark field (HAADF) STEM techniques are complementary for detailed analysis of this complex material. The information they display is compared in parts a and b of Figure 4. The HRTEM images provide characteristic contrasts on the formation of perovskite-type blocks separated by complex rows of tunnels, which can be directly compared to those observed in the ferrite $Pb_{18}Fe_{20}O_{48}$.[24] One example of a [010] enlarged HRTEM image is given in Figure 4b, with the high electron density zones appearing as the darker ones (focus close to −190 Å). At the level of the translational interface, a schematic drawing of the $Fe(Mn)O_6$ octahedra blocks is superposed on this experimental image, the six-sided tunnels, where the Pb^{2+} cations are likely located and are represented by white hexagons and the cations (Sr^{2+} and/or Pb^{2+}) located in the pentagonal cages by yellow circles. The interesting characteristic of the present CS structures with regard to the ferrites [24] deals with the presence of strontium and lead in the matrix, two cations with a significant difference in Z (Pb = 82 and Sr = 38), perfectly suited for HAADF STEM imaging. The intensity related to a column of atoms is indeed proportional to Z^n ($1 < n < 2$). The enlarged [010] HAADF STEM images of the present

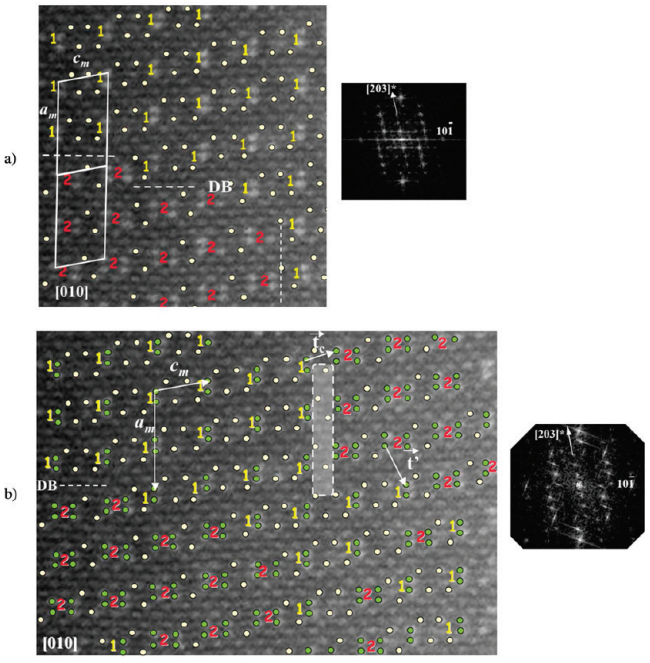

Figure 5. "Map" of the arrangement of the structural units in the translational interface, as obtained by the [010] HAADF STEM techniques (the phases "1" and "2" are labeled at the level of the interface). a) Enlarged image corresponding to a coherent boundary between the phases "1" and "2": the FFT evidences the alignment of the intense satellites with the basic reflections of the perovskite. b) Image characterized by different boundaries. The white shadowed zone corresponds to the defective boundary. The FFT evidences the misalignment and the decrease of intensity of the satellites.

material are characterized by zones of bright dots, which are associated with the cations located in the tunnels at the level of the translational interface. In Figure 4a, the brighter dots, i.e. higher Z, are correlated to the positions of the Pb^{2+} cations (green dots surrounded by a white hexagon) in the single and double tunnels H: one single hexagon associated with the phase "1" and two hexagons for the phase "2". In between two interfaces, the gray dots are correlated to the Sr^{2+} positions, and a possible minor amount of Pb^{2+} cations, located in the perovskite cages.

These HAADF STEM images provide a "map" of the distribution of the "higher Z" cations in the crystal, i.e. the relative arrangement of the different tunnels (double and single) along the interface. Two examples are given in Figure 5, in which the tunnels and pentagonal cages have been represented by green and white dots, respectively, and the nature of the phase "1" or "2" is mentioned to evidence the different domains and the arrangement of the different structural units in the interface. The enlarged image in Figure 5a corresponds to part of a crystallite where the adjacent domains "1" and "2" exhibit a perfect translation of the cell along $\vec{a}_m$ as well as along $\vec{c}_m$ over the domain boundaries (white dotted line). The associated Fast Fourier Transform FFT of these domains exhibiting coherent boundaries confirms that a unique commensurate pattern is obtained with satellites aligned along the $[10\bar{1}]^*_p$ direction. In Figure 5b, different boundaries are observed, and the FFT of this region shows an incommensurate modulation similar to that of Figure 3b despite the HAADF STEM "map" evidences only the presence of these two phases. The

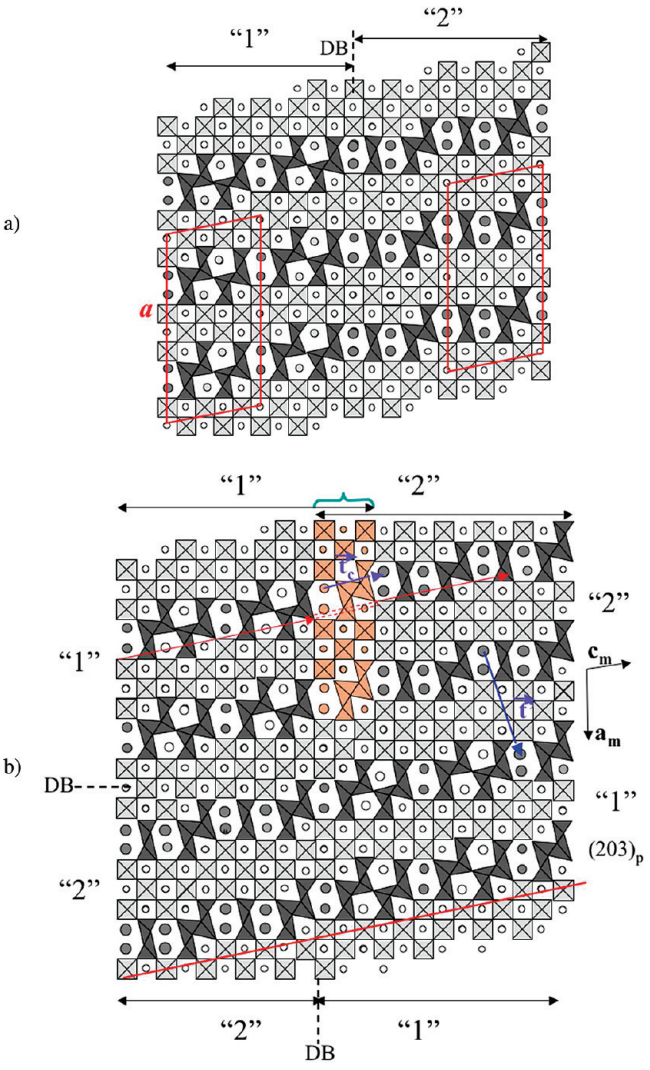

Figure 6. a) Coherent boundary "1" → "2" schematically projected along [010]. b) Topological representation of the different coherent boundaries and the additional vectors of translation associated with the discommensuration in the defective junction "1" → "2".

origin of the discommensuration should be therefore connected to these different types of junction between the "1" and "2" domains.

Origin of the Discommensuration. To determine the origin of the discommensuration, we should consider the expected sequences of the structural units along $\vec{c}_m$. They are [-tunnel-B_4O_{14}-B_4O_{14}]... for the phase "1" and [tunnel-B_2O_8-tunnel-B_4O_{14}]... for the phase "2". The different junctions observed in the experimental images (Figure 5) are schematically drawn in Figure 6.

- *coherent domain boundary* (DB): in the commensurate structure (dotted lines in Figure 5a), the translation $\vec{c}_m$ is respected, and the sequence of the junction [phase "2"] → [phase "1"] is

[tunnel-B_2O_8-tunnel-B_4O_{14}][-tunnel-B_4O_{14}-B_4O_{14}]

A coherent domain boundary (DB), the junction of the "2" and "1" phases ensures the periodicity so that the interface remains perfectly parallel to $(203)_p$ (Figure 6a). In the left part, the junction between the two phases

"1" → "2" along $\vec{a}_m$ is also perfectly ensured. This is observed in Figure 5(a and the left part of b), with a translation vector ($\vec{a}_m/2 + \vec{c}_m/2$) of the equivalent part of the two structures through the (DB) parallel to $(101)_p$. This is the expected arrangement in a commensurate structure, as shown from the FFT (Figure 5a) associated with this part of the image.

In a "defective" boundary (white shadowed rectangular zone in Figure 5b), the sequence is

[-tunnel-B_4O_{14}-B_4O_{14}-*tunnel-*B_4O_{14}-tunnel-
B_2O_8-tunnel-B_4O_{14}-tunnel-B_2O_8-tunnel-B_4O_{14}-]

The five first units [tunnel-B_4O_{14}-B_4O_{14}-*tunnel-*B_4O_{14}] correspond to the correct units sequence in the phase "1". However, the following units [*tunnel-*B_4O_{14}-tunnel-B_2O_8-tunnel-B_4O_{14}-tunnel-B_2O_8-tunnel-B_4O_{14}-] also adopt a correct sequence expected in the phase "2". In fact, one part of the sequence [-*tunnel-*B_4O_{14}] is consistent with a normal sequence of each of the two phases but is "abnormal" in a coherent sequence of junction phase "1" → phase "2". This group [-*tunnel-*B_4O_{14}], belonging to both domains at the level of the junction involves a translation $\vec{t}_c \neq \vec{c}_m$ between the two domains "1" and "2".

Topological Model of the Defective Boundary. In the top part of the image (Figure 6b), the above-mentioned sequence of the structural units and an overlap of the two phases (see the double arrows) are drawn. The common [*tunnel-*B_4O_{14}] unit in the translational interface (colored in orange) is associated with a block of four iron octahedra in the perovskite slice (the fifth polyhedron of the perovskite block being one of the pyramids of the B_4O_{14} unit). The modulation vectors of the two domains remain parallel to $(203)_p$ but are not collinear; they suffer a translation, which is outlined in Figure 6b by two rows of dotted lines. As a result, the defective boundary can be regarded as built up from the common structural group, i.e. [*tunnel-*B_4O_{14}] and the associated octahedra, locally shared by the phases "1" and "2". This structural group can be considered as built on the $\vec{t}_c$ and $\vec{a}_m$ vectors (see Figures 5 and 6), defining a monoclinic cell, with $a_{102} = a_m$ ($a_{102} \sin\beta \approx 5a_p\sqrt{2}$), $b_{102} \approx b_m \approx a_p$, $c_{102} = |\vec{t}_c|$, and $\beta_{102} \approx 108°4$; it corresponds to a $1/2[101](102)_p$ CS perovskite related structure with the theoretical composition $Sr_{10}Pb_4Fe_{16}O_{38}$ (or $(Sr_{0.71}Pb_{0.25})FeO_{2.375}$ per perovskite unit).

The formation of such defective boundaries through structural units common to the two phases is susceptible to involve additional translations along $\vec{c}_m$, in the adjacent domains. One example is given in Figures 5 and 6, with two vectors $\vec{t}_c$ and $\vec{t}$' which also lead to a misalignment of the cells along $\vec{a}_m$. This is observed in the image of Figure 5b and illustrated in the right part of Figure 6, with $\vec{t}' = \vec{a}_m/2 + \vec{b}_m/2 + \vec{c}_m/2$.

These local translations by $\vec{t}_c$ and $\vec{t}$' provoke ruptures in the translation in the interface with resulting displacement vector R, responsible for the incommensurate character observed in the diffraction patterns (see the FFT). The different experimental values of the component of the modulation vectors ($p\vec{a}^* + r\vec{c}^*$) are a function of the nature and the number of boundaries in the area selected in the microscope.

The simple drawing in Figure 6a shows that the junctions between the two phases can be coherent from a crystallographic point of view. They are therefore susceptible to generate perfect phasoid compounds with nanophases exhibiting only 3D coherent boundaries according to different arrangements, from a "disordered" model up to ordered intergrowths of the two phases "1" and "2", along $\vec{a}_m$ as well as along $\vec{c}_m$. If the latter ones can be stabilized, the commensurate supercell of these as-built intergrown phases would have a peculiar character, with the *a* or *c* parameter being an integer multiple of the a_m or c_m of only one mother cell, instead of two in the common intergrowth structures.

Chains as Structural Building Units (SBU) in the $1/2[110]_p(hkl)_p$ CS Structures. *CS Structures of the Fe-22(m-1)m Members*. The phases "1" and "2" can be considered as the two possible limit ordered states, observed in the form of nanophases, of the average phasoid compound $Sr_{16}Pb_4(Fe,Mn)_{26}\mathbf{M}_4O_{63\pm\varepsilon}$.[28] To understand the relationship between the complex structures of these cation deficient perovskites and the mechanism responsible for the discommensurations, we shall start from one of the simplest ferrites $SrFeO_{2.5}$.

This anion deficient $SrFeO_{2.5}$ ferrite[13] is an ordered brownmillerite, but, as soon as a cation deficiency is observed ($Sr_{1-x}FeO_{2.5-y}$ with $0 < x < 0.33$), ED shows that the perovskite-like framework is destroyed. The samples are multiphased with the coexistence of $SrFeO_{2.5-x}$ and different ferrites Fe-22(m-1)m, each **m** member having the composition $Fe_2(Sr_2)Sr_{m-1}Fe_mO_{2.5m+4.5-\delta}$[31,32] (Figure 1a). Following the approach proposed for the Aurivillius family by Boullay et al.,[33] these phases can be regarded as $1/2[110]_p(001)_p$ CS structures, the double Bi layers of the latter being replaced by double iron layers. The periodicity between the shear planes is directly related to **m** and therefore to the ratio Sr/Fe. To illustrate the $1/2[110]_p(001)_p$ CS character of these Sr rich ferrites, the idealized structure of the $\boldsymbol{m} = \mathbf{2}$ member[20] is drawn in Figure 7a: along $\vec{c}_p$, finite chains of two octahedra bordered by two pyramids are observed and translated by $\vec{a}_p$. The FeO_x polyhedra ($x = 5$ or 6) of these units share their corners along $\vec{a}_p$ and $\vec{c}_p$ in one slice, the junction between the slices is ensured through the pyramids in the translational interface. The $\boldsymbol{m} = \mathbf{3}$ member $Fe_2(Sr_2)Sr_2Fe_3O_{11.5-\delta}$ (or $Sr_{0.8}FeO_{2.3}$) is built up according to a similar mechanism from chains of three octahedra bordered by two pyramids (red colored in Figure 7b). According to this structural mechanism, the so-called terrace structure $Sr_{13}Pb_4Fe_{24}O_{58}$,[23] previously described as a complex intergrowth of Fe-2201 and Fe-2212

(31) Bredesen, R.; Norby, T.; Bardal, A.; Lynum, V. *Solid State Ionic* **2000**, *135*, 687.
(32) Mellenne, B. PhD Thesis, Caen, December 20th, **2005**.
(33) Boullay, Ph.; Trolliard, G.; Mercurio, D.; Perez-Mato, J. M.; Elcoro, L. *J. Solid State Chem.* **2002**, *164*, 252.

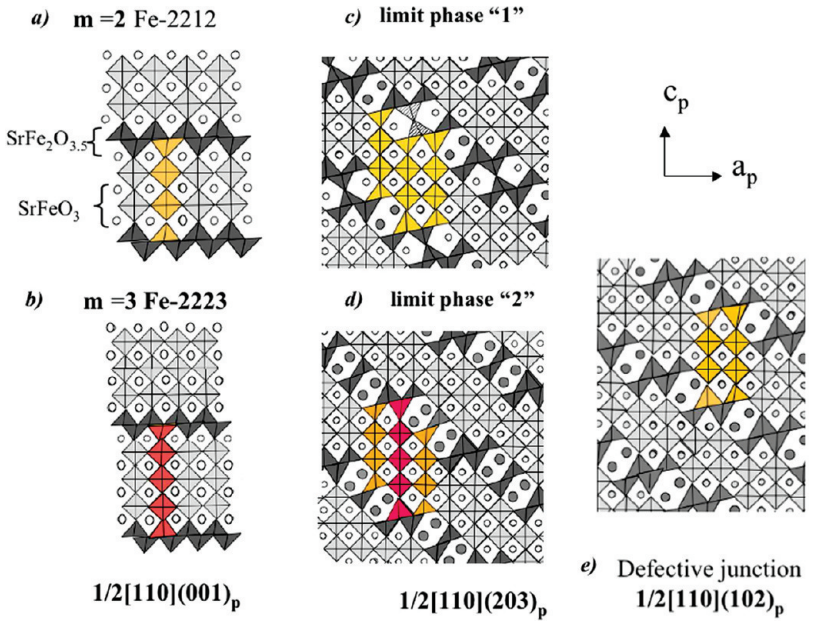

Figure 7. Structural building units: representation of five CS structures in the form of chains, parallel to $\vec{c}_p$, built of octahedra bordered by two pyramids forming the translational interface.

members, can also be reconsidered using a 3D shear vector as a $1/2[110]_p(111)_p$ CS structure.

The A/B Ratio. Thus, different $1/2[110]_p(hkl)_p$ CS structures are observed in a rather small existence domain of the Pb−Sr−Fe(Mn)−O diagram (Figure 1a); they differ by the form of the tunnels and cages managed in the framework and the nature of the cations located in it. In the $Pb_{4m+3n}Fe_{4(m+n)}O_{10m+9n}$ CS structures,[24−26] the perovskite cages and pentagonal and hexagonal tunnels are indeed only occupied by Pb^{2+}, whereas in the $Fe_2(Sr_{2-y}A_y)Sr_{m-1}Fe_mO_{3m+3.5-\delta/2}$ CS[17−22] and terrace[23] structures, Fe^{3+} is also located in the sites of the rock salt blocks with Sr^{2+} and Pb^{2+}. It appears that the two CS structures characterized by the lowest (Sr+Pb)/(Fe+Mn) ratio do not exhibit six-sided tunnels: namely the Fe-2201 phase $(Sr_{2/3-x}Pb_x)FeO_{2.167}$[23] and the "terrace" structure $(Sr_{0.54}Pb_{0.17})FeO_{2.21}$[23] (respectively dark pink and orange in Figure 1a). This analysis shows that the stabilization of the six-sided tunnels requires a higher A/B cation ratio.

The Chains as Structural Building Units. The two $1/2[110]_p(203)_p$ CS structures constituting the phasoid $(Sr_{0.61}Pb_{0.18})(Fe_{0.75}Mn_{0.25})O_{2.29}$ can be described using other SBU, which do not especially characterize the translational interface but the whole structure. These SBU are the chains of octahedra, parallel to $\vec{c}_p$ and bordered by two pyramids; different structures are drawn in Figure 7 to outline the nature and arrangement of these SBU. As above-mentioned, the $1/2[110]_p(001)_p$ CSS of the Fe-2212 (Figure 7a) and the Fe-2223 member (Figure 7b) are built up of chains of two and three octahedra, respectively. In Figure 7d, the limit "phase 2" of the $1/2[110]_p(203)_p$ CS structure is built from two chains of two octahedra (yellow colored, similar to those observed in the Fe-2212 phase) alternating with one chain of three octahedra bordered by two pyramids (similar to those observed in the Fe-2223 phase). The limit "phase 1" of the $1/2[110]_p(203)_p$ CS structure is also built from two chains of two octahedra bordered by two pyramids (yellow colored, as observed in the phase "2" and the Fe-2212 phase) alternating with a third chain, which can be described by one chain of two octahedra bordered by two pyramids and one shifted unit of two pyramids (hatched in Figure 7c), which manages pentagonal tunnels.

The study of the defective junctions between the nanodomains "1" and "2" showed that they result from the sharing of one common structural group related to the $1/2[110]_p(102)_p$ CS structure unit cell. The structure of the $1/2[110]_p(102)_p$ CS structure can be also described as built of only from the SBU consisting of two octahedra bordered by two external pyramids (Figure 7e).

The mechanism of junction of these chains is similar to the one described for the $1/2[110]_p(001)_p$ CS structure: the pyramids and octahedra of adjacent chains are corner sharing along $\vec{a}_p$ and $\vec{c}_p$, forming "perovskite" slices parallel to $(h0l)_p$; the junction between the slices is ensured through the external pyramids of each chain by a translation $(\vec{a}/2 + \vec{b}/2)$ but leads to the formation of distorted cages or five- and six-sided tunnels at the level of the interface.

Origin of This Defective Junction. Considering the investigated part of the diagram, it appears that the chains of two octahedra bordered by two pyramids is a structural building unit observed in the different CS structures of the pseudoternary diagram (Pb)−Sr−Fe−O (Figure 1a): the Fe-2212,[20] the $1/2[110]_p(102)_p$, the $1/2[110]_p(\bar{1}01)_p$,[15] and the $1/2[110]_p(\bar{3}05)_p$ (ref 24 and Figure 1c) CS structures. The fact that this unit is a membership of all these CS structures suggests its easy formation, which could be one of the important structural keys.

The second hypothesis is linked to a chemical factor correlated to the actual average composition $Pb_5Sr_{17}(Fe_{21}Mn_7)O_{63\pm\varepsilon}$, as determined by the EDS analysis of numerous crystallites[28] and the general formula of the

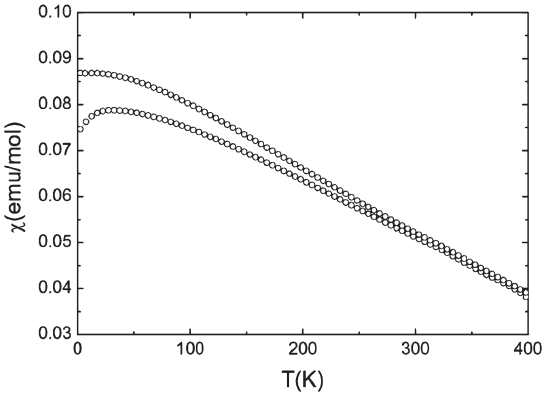

Figure 8. M(T) curves recorded in ZFC and FC modes, under a field of 0.3 T.

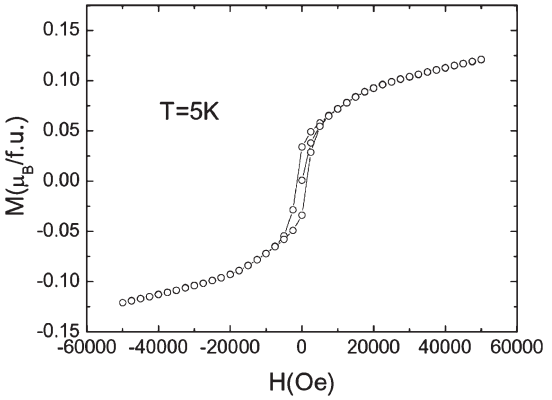

Figure 9. M(H) loop recorded at 5 K.

phasoid, $Pb_4Sr_{16}(Fe,Mn)_{26}\mathbf{M}_4O_{63\pm\varepsilon}$ with M being any cation of the framework (Figure 2b). Three theoretical limits of this formula draw a triangle represented in Figure 1a (long and short dotted lines); the $1/2[110]_p$-$(203)_p$ phase "2" $Sr_{16}Pb_8(Fe,Mn)_{26}O_{63}$ and the $1/2[110]_p$-$(203)_p$ phase "1" $Sr_{18}Pb_4(Fe,Mn)_{28}O_{64}$ CS structures are two of its limits, but, from the compositional point of view, another one is the Pb-rich limit of the Fe-2201structure $1/2[110]_p(001)_p$ CSS, with $M_4 = Sr_4$, $Pb_4Sr_{20}Fe_{26}O_{63}$. This remark supports the aforementioned one about the important role of the A/B ratio on the stabilization of the different types of tunnels. The actual average composition of the phasoid $Pb_5Sr_{17}(Fe_{21}Mn_7)O_{63\pm\varepsilon}$ (red star in Figure 1a) is in the center of this triangle; this is expected considering the two theoretical limit models, Pb_4Sr_{18}-$(Fe,Mn)_{28}O_{64}$ for the phase "1" and $Pb_8Sr_{16}(Fe,Mn)_{26}O_{63}$ for the phase "2" (blue stars in Figure 1a), because it is consistent with the HRTEM and HAADF STEM images.

The chemical and structural factors, with the common SBU of two octahedra bordered by two pyramids belonging to structures very close in composition could explain the easy formation of the defective junctions (and therefore the discommensuration) phenomena.

Magneto-Transport Properties. Figure 8 presents the magnetization measured under 0.3 T, both in zero field cooled and field cooled modes. The value of magnetization is small, close to 0.08 emu/mol at 5 K, and the two curves are separated almost in the whole T range. Also, the value of susceptibility at 400 K is still different from zero. These two experiments point to a transition temperature above 400 K. This of course prevents any Curie−Weiss-like analysis of the susceptibility.

Figure 9 presents the M(H) loop recorded at 5 K. Under high magnetic field (5 T), the magnetization remains very small, with 0.12 μ_B/f.u. A small hysteresis is observed, with a coercive field close to 1000 Oe. A similar behavior is observed at high T, and the hysteresis is still observed at 300 K, with a smaller value of the magnetization in 5 T (0.08 μ_B/f.u. instead of 0.15 at 5 K). This small magnetization is associated with an insulating behavior, with $\rho > 10^6\ \Omega$.cm at 300 K.

The small values of magnetization measured here and the likely high value of the transition temperature indicate a strong antiferromagnetic behavior in these oxides. This behavior is typically observed in related structures such as "terrace" structure, in $Pb_4Sr_{13}Fe_{24}O_{53}$.[23] The 180° Fe^{3+}−O−Fe^{3+} interactions are strongly antiferromagnetic with, e.g. $T_N = 750$ K in $LaFeO_3$.[34] Compared to previous results, a very small hysteresis is observed on the M(H) loop. The difference with the previously investigated structures is the substitution of Mn^{3+} for Fe^{3+} and the formation of tunnels, which cut the $[BO_2]_\infty$ perovskite-type planes in the translational interface. Following the Kanamori-Goodenough rules, for 180° Mn^{3+}−O−Fe^{3+} superexchange can be AFM or FM.[35] Calculations have shown that the superexchange interactions should be antiferromagnetic.[36] In perovskites, the Mn^{3+}−O^{2-}−Fe^{3+} interactions are reported to be strongly AFM.[37] However, in most cases, these results are obtained in iron doped manganese perovskites with a mixed Mn^{3+}/Mn^{4+} valency. For pure Mn^{3+} and Fe^{3+}, there are only a few reports. The introduction of Mn^{3+} in $BiFeO_3$ was used as a way to induce ferromagnetic interactions.[38−40] It was shown that magnetization increases as x increases, and a small hysteresis can be obtained in $BiFe_{1-x}Mn_xO_3$ for $x > 0.1$.[39] The value of the coercive field is close to 1000 Oe, and the magnetization obtained at 5 T and 10 K for $x = 0.3$,[39] i.e. roughly the same Fe^{3+}/Mn^{3+} ratio as in $(Sr_{0.61}Pb_{0.18})(Fe_{0.75}Mn_{0.25})O_{2.29}$, is similar to the one observed in Figure 9, close to 1000 emu/mol. Compared to $BiFe_{1-x}Mn_xO_3$,[38,39] not only octahedral but also pyramidal environments have to be considered and could also play a role on the appearance of hysteresis. A complete understanding of the magnetic structure is still lacking, but the appearance of hysteresis could also be due to FM interactions between Mn^{3+} and Fe^{3+}.

(34) Koehler, W. C.; Wollan, E. O.; Wilkinson, M. K. *Phys. Rev.* **1960**, *118*, 58.
(35) Goodenough, J. B. *Phys. Rev.* **1955**, *100*, 564.
(36) Sherman, D. M. *Am. Mineral.* **1990**, *75*, 256.
(37) (a) Leung, L. K.; Morrish, A. H.; Evans, B. J. *Phys. Rev.* **1976**, *B13*, 4069. (b) Simopoulos, A.; Pissas, M.; Kallias, G.; Devlin, E.; Moutis, N.; Panagiopotoulos, I.; Niarchos, D.; Christides, C.; Sonntag, R. *Phys. Rev.* **1999**, *B59*, 1263. (c) Troyanchuk, I. O.; Bushinsky, M. V.; Szymczak, H.; Baran, M.; Bärner, K. *J. Magn. Magn. Mater.* **2007**, *312*, 470.
(38) Yang, C−H.; Koo, T. Y.; Jeong, Y. H. *Solid State Commun.* **2005**, *134*, 299.
(39) Sahu, J. R.; Rao, C. N. R. *Solid State Sci.* **2007**, *9*, 950.
(40) Azuma, M.; Kanda, H.; Belik, A. A.; Shimakawa, Y.; Takano, M. *J. Magn. Magn. Mater.* **2007**, *310*, 1177.

Concluding Remarks

A detailed analysis of the FFT taken from HRTEM and HAADF-STEM images of adjacent domains exhibiting coherent boundaries parallel to $(100)_m$ and/or $(001)_m$ shows that they lead to commensurately modulated ED patterns. Moreover, these techniques allow to evidence that the incommensurability phenomena are associated with the formation of defective boundaries through structural units groups, [(*tunnel-B_4O_{14}*) and associated octahedra], which are a common part of the normal sequences encountered in the variants "1" and "2". The presence of these common structural unit groups leads to a misalignment of the "1" and "2" monoclinic supercells along $\vec{a}_m$ and are susceptible of involving additional translations along $\vec{c}_m$, in the adjacent domains. These local translations provoke ruptures in the periodicity and are responsible for the incommensurability observed in the diffraction patterns. The experimental values of the modulation vectors ($p\ \vec{a}^* + r\ \vec{c}^*$) are a function of the nature and the number of boundaries in the area selected for obtaining the diffraction pattern.

The analysis of the CS phases in the Pb−Sr−Fe-(Mn)−O diagram has shown that the stabilization of the six-sided tunnels requires a higher A/B cation ratio and is allowed to propose a new mode for describing these CS structures. They are built up from simple chains, running along $\vec{c}_p$, of octahedra bordered by two pyramids; the adjacent chains share their polyhedra corners along $\vec{a}_p$ and $\vec{c}_p$, to form "perovskite" slices parallel to $(h0l)_p$ and the junction between the slices is ensured through the external pyramids of each chain leading to the formation of distorted cages or five- and six-sided tunnels at the level of the translational interface. This model allows the understanding of the relationship between the variants observed in the phasoid $1/2[110]_p$-$(203)_p$, the $1/2[110]_p(001)_p$, the Fe-2212,[20] and the $1/2[110]_p(102)_p$ CS structures.

The strong antiferromagnetic and insulating behavior is very similar to the one obtained for other CS ferrites of the system.[23,29] The evidence of a hysteresis, with a small coercive field, reflects interesting magnetic properties; the investigation of these new materials is in progress.

Acknowledgment. The authors acknowledge financial support from the European Union under the Framework 6 program under a contract for an Integrated Infrastructure Initiative (Reference 026019 ESTEEM).